Chemical Science

ROYAL SOCIETY OF CHEMISTRY

EDGE ARTICLE

View Article Online
View Journal | View Issue

Cite this: *Chem. Sci.*, 2022, **13**, 12840

All publication charges for this article have been paid for by the Royal Society of Chemistry

Plasmon enhanced catalysis-driven nanomotors with autonomous navigation for deep cancer imaging and enhanced radiotherapy†

Luntao Liu,‡[a] Qingqing Li,‡[a] Lanlan Chen,*[a] Lihong Song,[b] Xueqiang Zhang,[b] Hongqi Huo,[b] Zhixin You,[b] Ying Wu,[a] Zongsheng Wu,[a] Jiamin Ye,[a] Qinrui Fu,[a] Lichao Su,[a] Xuan Zhang,[a] Huanghao Yang[a] and Jibin Song*[a]

Received 31st May 2022
Accepted 13th August 2022

DOI: 10.1039/d2sc03036e

rsc.li/chemical-science

Radiosensitizers potentiate the radiotherapy effect while effectively reducing the damage to healthy tissues. However, limited sample accumulation efficiency and low radiation energy deposition in the tumor significantly reduce the therapeutic effect. Herein, we developed multifunctional photocatalysis-powered dandelion-like nanomotors composed of amorphous TiO_2 components and Au nanorods (~93 nm in length and ~16 nm in outer diameter) by a ligand-mediated interface regulation strategy for NIR-II photoacoustic imaging-guided synergistically enhanced cancer radiotherapy. The non-centrosymmetric nanostructure generates stronger local plasmonic near-fields close to the Au–TiO_2 interface. Moreover, the Au–TiO_2 Schottky heterojunction greatly facilitates the separation of photogenerated electron–hole pairs, enabling hot electron injection, finally leading to highly efficient plasmon-enhanced photocatalytic activity. The nanomotors exhibit superior motility both *in vitro* and *in vivo*, propelled by H_2 generated *via* NIR-catalysis on one side of the Au nanorod, which prevents them from returning to circulation and effectively improves the sample accumulation in the tumor. Additionally, a high radiation dose deposition in the form of more hydroxyl radical generation and glutathione depletion is authenticated. Thus, synergistically enhanced radiotherapeutic efficacy is achieved in both a subcutaneous tumor model and an orthotopic model.

Introduction

Radiotherapy (RT), with high optical penetration depth and precise disease localization, is widely employed in the clinic to combat cancers by locally conferring X-rays or γ-rays onto tumors to produce reactive oxygen radicals (ROS) and induce DNA damage to achieve antitumor activity.[1–5] Unfortunately, its therapeutic effect is not always satisfactory, primarily due to the severe hypoxia-induced radiation resistance of tumor cells and high dosage of radiation energy extremely harmful to normal tissues.[6–9] Recent advances in developing high atomic number (*Z*) nanoparticles (*e.g.*, gold, iodine, gadolinium, bismuth, rare earth elements, and metallic oxides) as radiosensitizers have contributed to potentiating the therapeutic efficacy of RT.[10] Nevertheless, most single-component radiosensitizers present a low radiation dose deposition due to their limited charge separation and migration. Hybrid nanostructures with various functional materials within the same structures endow them with heterojunctions,[11] significantly facilitating the charge separation and migration to boost the radiosensitization effects.

In addition to the low radiation dose deposition, the limited accumulation and uneven distribution of radiosensitizers in the tumor is another obstacle which significantly affects the radiotherapeutic efficacy. Generally, nanomedicines accumulate primarily on the tumor surface *via* the extravasation of fenestrated blood vessels and then penetrate deep tissues through passive diffusion. However, the harsh tumor environment (*e.g.*, densely packed tumor cells, insufficient blood supply, and high extracellular fluid pressure) makes it difficult for samples to penetrate the inner tumor area only through passive diffusion, even causing most samples accumulate on the tumor surface to diffuse back into circulation.[12,13] Although diverse new strategies (*e.g.*, peptide-based transcellular transport, smart switching of size, shape, and surface charge of nanomedicines, and the modulation of the tumor structure and environment) have been developed to enhance sample accumulation and distribution in the tumor,[14–16] the penetration ability of radiosensitizers relying on passive diffusion is not gratifying.

Artificial micro/nanomotors, since their introduction in 2005, have become a powerful dynamic tool in the biomedical field to

[a]*MOE Key Laboratory for Analytical Science of Food Safety and Biology, College of Chemistry, Fuzhou University, Fuzhou 350108, China. E-mail: chem4@163.com*

[b]*Department of Nuclear Medicine, Han Dan Central Hospital, Handan, 056001, Hebei, China*

† Electronic supplementary information (ESI) available. See DOI: https://doi.org/10.1039/d2sc03036e

‡ Luntao Liu and Qingqing Li contributed equally to this work.

accomplish various complex tasks at the micro- or nanoscale, including active drug delivery, antibacterial activity, *in vivo* imaging, and disease treatment.[17–19] They can effectively convert diverse chemical energy or external stimuli into kinetic force to achieve autonomous movement, showing great promise for passing through biological barriers to facilitate tissue penetration.[20–22] The motors' asymmetrical structure plays a crucial role in directional movements.[23,24] For clinical applications, the Janus structure design is essential and should be as simple as possible, and the performance should be tailored to cancer applications while ensuring functional synergies among incorporated multiple components.[25] At present, multifunctional micro/nanomotors are applied to treat diverse diseases such as diabetes, bacterial infections, ischemic stroke, and thromboembolism, to name a few.[26–28] However, it is a significant challenge to extend the success to antitumor treatment, mainly due to their shape, composition, size, and toxic chemical fuel (*e.g.*, hydrogen peroxide, hydrazine, bromine, and iodine).[29–31] In particular, the miniaturization of artificial motors to an appropriate nanoscale, which is critical for *in vivo* biological applications, is a significant challenge.[32] Currently, most nanomotors are fabricated through physical processing technology.[33] In fact, developing robust chemical synthesis to fabricate Janus nanomotors on a large scale would be significant progress toward an actual clinical transformation of the motile system.

Photoacoustic imaging (PAI) has recently attracted considerable attention because it perfectly combines ultrasound imaging and optical imaging, with high contrast, deep tissue penetration, and sensitivity.[34–39] The optical absorber absorbs the laser pulse, and the energy is converted into heat, which induces thermal expansion; then, ultrasound waves are generated. It is well-established that gold nanorods (Au NRs) are a promising NIR-II PAI contrast agent due to their tunable aspect ratio, resulting in excellent optical absorption in the NIR-II region. In addition, they are also superior radiosensitizers that generate a great deal of short-range secondary electrons (*e.g.*, photoelectrons, diffused photons, Auger electrons, and fluorescence photons) with radiation exposure.[40]

The synergistic interaction between noble metals and a high dielectric semiconductor could produce extraordinary photoelectric properties. Inspired by plasmon-enhanced photocatalysis of noble metal/semiconductor hybrid nanomaterials, in this work we first constructed multifunctional photocatalysis-powered dandelion-like nanomotors composed of gold nanorods (Au NRs) and titanium dioxide nanoparticles (TiO_2 NPs) (denoted as AuNR-TiO_2 nanomotors) by a wet-chemistry synthesis for NIR-II photoacoustic imaging-guided synergistically enhanced cancer radiotherapy. The obtained Janus nanomotors show a unique dandelion-like structure, in which amorphous TiO_2 NPs anchor on one side of Au NRs with an apparent spatial separation architecture (Scheme 1a). Thanks to the interaction between Au NRs and TiO_2 components, resulting in superior optical absorption in the NIR-II window, the nanomotors could be used as a brilliant NIR-II PAI contrast agent for tracing their movement trajectory and guiding cancer therapy (Scheme 1b). The Janus nanomotors display significantly enhanced NIR-catalytic hydrogen evolution and high radiation energy deposition in the form of highly cytotoxic hydroxyl radicals (˙OH) and glutathione depletion.[41] This effect can be explained because the synergistic interaction between the noble metals and the high dielectric semiconductors generates strong near-fields close to the Au–TiO_2 interface, and the Au–TiO_2 Schottky heterojunction effectively facilitates charge separation and migration.[41,42] The generated H_2 at one end of the Au NRs serves as an effective driving force to propel the nanomotor forward to facilitate cell uptake and improve sample accumulation and distribution.[43,44] The excellent penetration capability of the nanomotors driven by their active

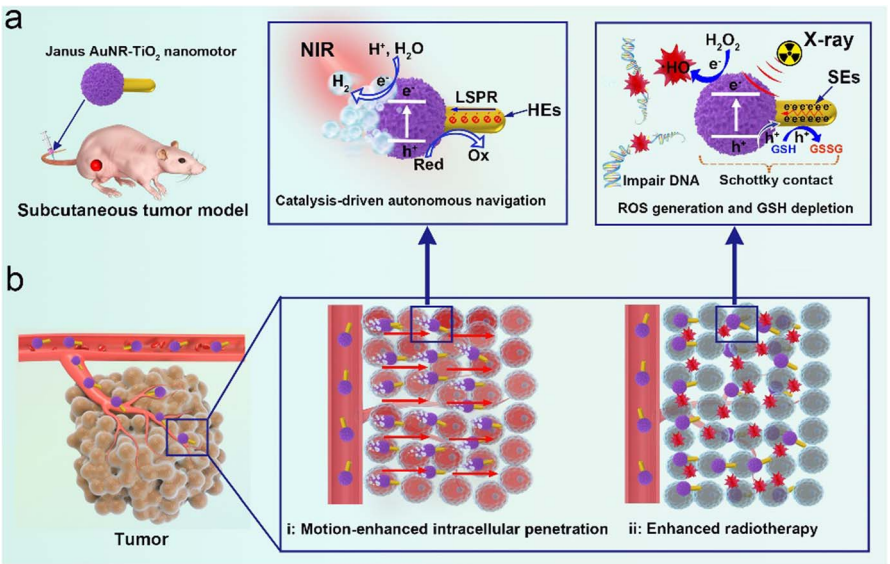

Scheme 1 Schematic illustration of the mechanism and application of AuNR-TiO_2 nanomotors. (a) The mechanism of plasmon-enhanced NIR-catalytic hydrogen evolution and Au–TiO_2 Schottky contact enhanced radiation dose deposition. (b) The application of nanomotors in enhanced cancer radiotherapy (HEs: hot electrons, SEs: secondary electrons).

motion has been confirmed *in vitro* and *in vivo*. The content of the nanomotors accumulated at the tumor site in the presence of NIR was approximately 1.8 times higher than that without NIR irradiation. Moreover, upon NIR irradiation, the nanomotor distribution in the tumor was more even. The synergistic enhancement of RT outcome of the nanomotors was authenticated in both a subcutaneous mice model and an orthotopic liver cancer model. This study presents a novel design of radiosensitizers, providing a new avenue for highly effective RT. We believe that such multifunctional Janus nanomotors will significantly promote the clinical application of RT.

Results and discussion

Preparation and characterization of Janus AuNR-TiO_2 nanomotors

To prepare Janus AuNR-TiO_2 nanomotors, uniform Au NRs measuring ~93 nm in length and ~16 nm in outer diameter were synthesized by a modified seed-mediated method (Fig. S1†).[45] During the procedure, 4-mercaptophenylacetic acid (4-MPAA) and poly(acrylic acid) (PAA) were controllably decorated on the surface of Au NRs, resulting in two distinct surface domains with different ligands. The PAA polymeric layer blocks the diffusion of tetraethyl orthosilicate (TEOS) to the surface of the Au NRs, while the carboxylic groups of 4-MPAA easily react with the silane monomer (monosilicic acid) (Fig. 1a). Therefore, the region anchored with 4-MPAA in Au NRs would deposit the SiO_2 component, while the region anchored with PAA is bare, resulting in Janus AuNR-SiO_2 nanostructures (Fig. 1b). The inert SiO_2 component in AuNR-SiO_2 nanostructures blocked the deposition of the TiO_2 component, but the bare gold region deposited the TiO_2 component successfully. Next, AuNR-SiO_2-TiO_2 nanostructures were synthesized by a bottom-up wet-chemistry strategy, using $NaHCO_3$ to tune the system's pH and further control the hydrolysis of $TiCl_3$ on the bare end of Au NRs (Fig. 1c). The TiO_2 component was successfully deposited on the

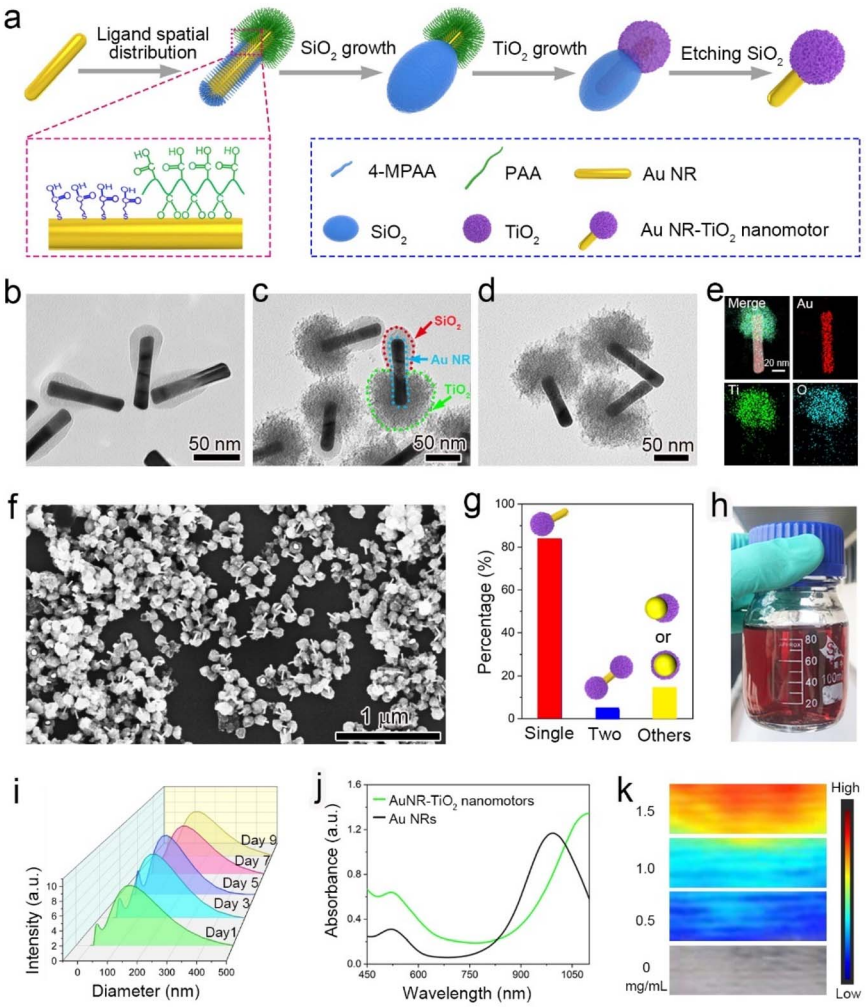

Fig. 1 Synthesis and characterization of the Janus AuNR-TiO_2 nanomotor. (a) Scheme of the synthesis of the nanomotor. TEM images of (b) asymmetric AuNR-SiO_2 nanostructures, (c) AuNR-SiO_2-TiO_2 nanostructures, and (d) Janus AuNR-TiO_2 nanomotors and (e) their element mapping. (f) The SEM image of the nanomotors. (g) The number percentage histogram of the dandelion-like, dumbbell-like or other shaped products in one pot. (h) The digital photograph of nanomotor aqueous dispersion (>80 mL). (i) Hydrodynamic size distribution of the nanomotors in nine days. (j) UV-vis-NIR absorption spectra of Au NRs and the nanomotors. (k) PA images of the nanomotor *vs.* its concentration.

gold surface of the AuNR-SiO_2 nanostructures (Fig. S2†). Ultimately, dandelion-like AuNR-TiO_2 nanomotors were obtained through etching the SiO_2 components with ammonia (Fig. 1d).

The typical asymmetrical nanostructure of the nanomotor was further identified by the element distribution mapping, wherein TiO_2 components are only distributed on one side of the Au NR (Fig. 1e). The statistical results of the number percentage of the products showed that the dandelion-like nanomotors, dumbbell-like nanoparticles and other shaped nanoparticles in one pot accounted for 83.5%, 11.4% and 5.1%, respectively, showing a high yield of the nanomotors (Fig. 1f and g). As shown in Fig. 1h, using this robust wet chemistry method more than 80 mL of nanomotor aqueous dispersion (OD value of ~2.0) could be obtained by one pot, significantly conducive to the clinical application. Furthermore, the Janus AuNR-TiO_2 nanomotors with different coverage percentages of TiO_2 components could be controllably synthesized by controlling the feed ratio of PAA and 4-MPAA. Keeping other experimental parameters unchanged, we used PAA alone to prepare the core/shell AuNR-TiO_2 nanostructure and defined it as 100% of TiO_2 coverage on the surface of Au NRs. Intriguingly, the TiO_2 coverage percentage was controlled from approximately 35.7 to 100% by decreasing 4-MPAA from 240 to 0 μL (Fig. 1d and S3†). This is because decreasing the feed ratio of 4-MPAA and PAA reduces the SiO_2 coverage percentage of the AuNR-SiO_2 nanostructure proportionately, leading to a corresponding increase in the TiO_2 coverage rate of the AuNR-SiO_2-TiO_2 nanostructure. Herein, the asymmetrical AuNR-TiO_2 nanomotors with approximately 35.7% of TiO_2 coverage percentage were treated as the typical samples to carry out the following experiments. The DLS analysis shows that these nanomotors are small enough to be employed in cancer treatment with a mean hydrodynamic size of approximately 120 nm and excellent structural stability within nine days (Fig. 1i). Since the introduction of TiO_2 components increases the refractive index around Au NRs, the absorption peak of the nanomotor aqueous dispersion exhibits a significant red-shift, extending to the NIR-II region (Fig. 1j). Accordingly, the PAI intensity of AuNR-TiO_2 nanomotors was enhanced significantly, which is 2.5 times than that of Au NRs (Fig. S4†). The nanomotors display strong PAI signals in the NIR-II window, and their PAI signal intensity increases in a concentration-dependent manner (Fig. 1k and S5†). Additionally, the AuNR-TiO_2 nanomotors under physiological mimicking conditions containing 10% FBS, PBS, or cell culture medium all showed good stability without observable aggregation and precipitation after one week (Fig. S6†).

Plasmon-enhanced photocatalysis-driven motion

To elucidate the underlying mechanisms of the enhanced photocatalytic activity of the Janus AuNR-TiO_2 nanomotors, the finite-difference-time-domain (FDTD) simulation was first conducted to confirm their plasmonic near-fields and optical absorption. As seen in Fig. 2a, the as-prepared dandelion-like nanomotors exhibit strong and asymmetric localized plasmonic near-fields at the Au–TiO_2 interface under 660 nm wavelength light irradiation, attributed to the higher refractive index at the Au–TiO_2 interface than that at the Au-aqueous interface. The nanomotors exhibit intense optical absorption close to the Au–TiO_2 interface due to the strong localized plasmonic near-fields (Fig. 2b). Fig. 2c depicts the corresponding plasmon-enhanced photocatalytic chemical reactions: (1) photogenerated electrons (e_{cb}^-) are excited from the valence band (VB) to the CB of the amorphous TiO_2 NPs by plasmon-induced resonance energy transfer (PIRET); (2) hot electrons (HEs) from the Au NRs are transferred to the TiO_2 components; (3) photogenerated holes (h_{vb}^+) cross the Schottky barrier to the reactive Au NRs; (4) the h_{vb}^+ are captured by sacrificial species (*e.g.*, GSH, lactic acid); (5) The surviving e_{cb}^- and the injected HEs jointly reduce H^+/H_2O to H_2. As shown in Fig. S7,† the hydrogen generation rate is approximately 14.2 ± 1.83 μmol g^{-1} h^{-1} under NIR laser irradiation (0.8 W cm^{-2}).

The photocatalytic activity of the nanomotors was further identified by catalytic degradation of methylene blue (MB). The absorption intensity of MB dye at 662 nm gradually decreases as a function of NIR irradiation time, with approximately 100% of MB being degraded after 14 min of irradiation (Fig. 2d).

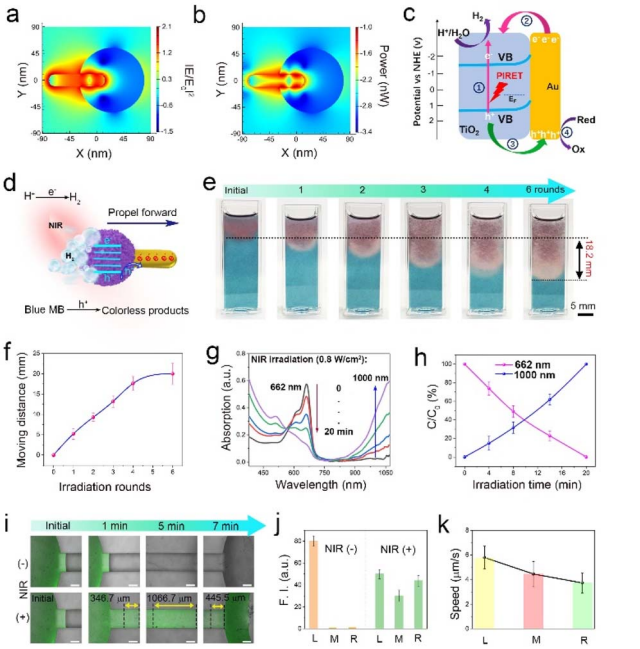

Fig. 2 Photocatalytic activity and motility of the Janus AuNR-TiO_2 nanomotors. (a) Plasmonic near-fields and (b) optical-absorption maps (cross-section view at $z = 0$) of the nanomotor simulated by the FDTD method. (c) Schematic diagram of the mechanism of LSPR-enhanced photocatalytic H_2 generation. (d) UV-vis-NIR spectra of the de-coloration process of the nanomotor/MB aqueous solution upon NIR laser irradiation. (e) Photographs of the nanomotors in agarose/MB hydrogel (0.05 wt%) moving downward under different rounds of NIR laser irradiation, and (f) the corresponding varying curve of moving distance *vs.* irradiation rounds. (g) UV-vis-NIR spectra of the nanomotors in agarose/MB hydrogel recorded at a distance of 8 mm from the starting position under NIR laser irradiation, and (h) the corresponding changing curves of the absorption intensity at 662 nm and 1000 nm, respectively. (i) CLSM images of the motility of nanomotors in a two-outlet microfluid channel, (j) the corresponding fluorescence intensity (F. I.), and (k) the velocity at different positions (scale bar: 200 μm).

Moreover, the degradation rate of MB dye increases in a laser power-dependent manner (Fig. S8†). The superior photocatalytic degradation performance of the nanomotors further indicates the effective separation of e_{cb}^- and h_{vb}^+. Subsequently, we investigated the photocatalysis-driven motion capability of the nanomotors in agarose hydrogel. Using MB dye as an indicator, 200 μL of nanomotors (4 mg mL^{-1}) were dropped at the top of a cuvette filled with agarose/MB hydrogel (0.05 wt%). Then NIR laser (0.8 W cm^{-2}) beams were irradiated vertically from top to bottom. Fig. 2e shows that parallel with an increase in the NIR irradiation rounds, the MB dye in the hydrogel is gradually degraded from top to bottom, with the color changing from blue to red. This indicates that the nanomotors move downward under the effect of the NIR laser irradiation, degrading MB dye around them simultaneously. Since five rounds of NIR irradiation were carried out (laser power: 0.8 W cm^{-2}, each irradiation round: 10 min, and the interval: 5 min), the motion distance of the nanomotors in the cuvette was around 18.2 mm, indicating a motile velocity of approximately 5.06 μm s^{-1} (Fig. 2f). Additionally, it is noteworthy that no significant heat effect was observed in the AuNR-TiO_2 nanomotor group after continuous irradiation for 10 min (Fig. S9†). We monitored the spectral changes of the system at a distance of 8 mm from the starting position to further study the movement behavior of the nanomotors. Note that as the NIR irradiation rounds increased, the absorption intensity of the system at 662 nm decreased gradually, and in turn, the absorption intensity at 1000 nm continuously increased (Fig. 2gand h). This further implies that the nanomotors pass through the agarose hydrogel barrier and keep moving downward driven by NIR laser beams. In contrast, the system's color and absorption spectra at a distance of 8 mm from the starting position remained almost unchanged without NIR irradiation (Fig. S10†).

A two-outlet microfluid channel was used to further evaluate the motility of the AuNR-TiO_2 nanomotor by confocal laser scanning microscopy (CLSM). Nanomotors marked with fluorescent FITC-PEG-SH (green) were dropped into the left chamber of the microfluid channel, and the NIR laser beams irradiated the channel from left to right horizontally, as illustrated in Fig. S11.† Significant amounts of bright green fluorescent spots appeared in the middle and right positions of the channel upon NIR irradiation. In contrast, no significant green fluorescent signals were observed in the absence of NIR irradiation (Fig. 2i). Accordingly, the fluorescence intensity both in the middle and the right positions increased significantly upon NIR irradiation, indicating that the nanomotors successfully moved towards the right position (Fig. 2j). The velocities of the nanomotors in the left, middle, and right positions are ~5.78, ~4.44, and ~3.71 μm s^{-1}, respectively (Fig. 2k).

Penetration behavior in a cellular environment

The penetration ability of AuNR-TiO_2 nanomotors enhanced by active motion was studied in a cellular environment. As shown in Fig. 3a, human Michigan Cancer Foundation-7 (MCF-7) cells served as cell models, the nuclei were labeled with HOE33342 (blue), and the nanomotors were marked with FITC-PEG-SH (green). A very weak green fluorescence was observed in the absence of NIR irradiation. In contrast, remarkable green fluorescence was observed with NIR irradiation (irradiation time: 8 min, the interval: 20 min, and the power: 0.8 W cm^{-2}), and the F. I. increased as a function of irradiation rounds (Fig. 3a–c). These results imply that the motion of the nanomotors significantly facilitates cellular internalization. The effects of motion on cellular internalization of the samples were further explored by quantitatively analyzing the cellular internalization efficiency of the Au NRs or the nanomotors with different NIR irradiation rounds. As shown in Fig. 3d, the cellular internalization efficiency in both Au NRs + NIR and the nanomotor – NIR groups was relatively low. In contrast, in the nanomotor + NIR group, it increased significantly from approximately 10.8 to 23.6%, with the NIR irradiation rounds increasing from 0 to 5 (Fig. 3d). The significantly enhanced internalization efficacy further suggests the positive effects of motion from nanomotors on cellular internalization.

The above findings were evaluated based on the cellular model. Herein, 3D MCF-7 MCSs were constructed to simulate the *in vivo* solid tumor model and further determine the penetration ability of the nanomotors into the tumor. In Fig. 3e, apparent green fluorescence was observed at a *z*-axis distance of 20 μm. In the absence of NIR laser irradiation, the green fluorescence reduced significantly as a function of scanning depth, and the fluorescence almost disappeared at a scanning depth of 80 μm. In contrast, in the presence of NIR irradiation (three rounds of NIR irradiation), strong green fluorescence covered the entire spheroid even at 120 μm scanning depth, implying that active motion of the nanomotors could assist them in entering the cells and realizing deep 3D MCS penetration by cell-to-cell transport (Fig. 3f and S12†). Additionally, we investigated the mechanism of the effects of motion of the nanomotors on their enhanced penetration and intracellular distribution by means of cellular co-localization with lysosomes marked with LysoTracker Red (red), nucleus labeled with HOE3342 (blue) and nanomotors decorated with FITC-PEG-SH (green). As for the NIR irradiation group, a tremendous amount of nanomotors were distributed in both lysosomes and nucleus (Fig. 3g). The corresponding F. I. curves more clearly display that some of the green fluorescence signals (nanomotors) coincided with red fluorescence (lysosome), while some green and blue fluorescence signals coincided with each other, implying that NIR irradiation assists nanomotors in escaping from lysosomes and gathering around the nucleus. In contrast, in the absence of NIR irradiation, green fluorescence signals almost coincided with red fluorescence, indicating that most nanomotors were retained in lysosomes (Fig. 3h). The motion ability of the nanomotors could promote their escape from lysosomes and assist them in gathering around the nucleus, conducive to impairing DNA and inducing cell apoptosis.

Radiation-induced chemical reactions

In addition to serving as an active delivery vehicle, the AuNR-TiO_2 nanomotor was also studied as a promising

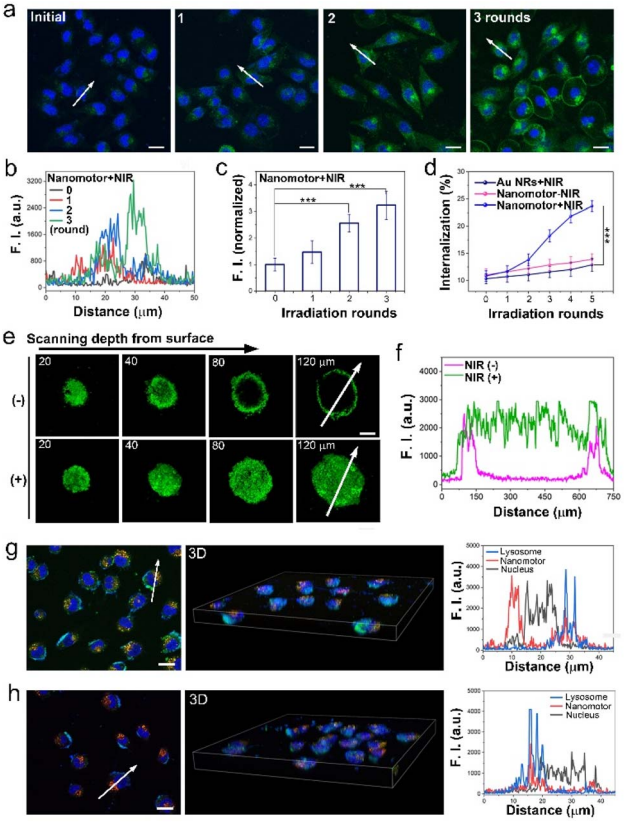

Fig. 3 Penetration ability of Janus AuNR-TiO_2 nanomotors in cells and 3D MCSs. (a) CLSM image, (b) corresponding fluorescence curves, and (c) histogram of quantitative comparison of fluorescence intensity (F. I.) of the MCF-7 cells co-incubated with nanomotors after different rounds of NIR laser irradiation (the whole incubation time was 2 h, scale bar = 20 μm). (d) Curves of cellular internalization efficiency of the samples *vs.* irradiation times. (e) Z-scanning CLSM images of the *in vitro* penetration of the nanomotors into MCF-7 MCSs after four rounds of NIR irradiation, and (f) the F. I. profiles at a scanning depth of 120 μm. Colocalization of nanomotors (green) with LysoTracker Red (lysosome, red) and HOE3342 (nucleus, blue) after MCF-7 cells being co-incubated with nanomotors (g) upon three rounds of NIR laser irradiation or (h) without NIR treatment and corresponding F. I. curves (the whole incubation time = 2 h). Scale bar: 20 μm, statistics analysis: $*p < 0.1$, $**p < 0.01$, $***p < 0.001$.

radiosensitizer, *i.e.*, a movable radiosensitizer. The radiosensitization effects strongly depend on the reaction between photons and matter. Upon collision with matter, the photon energy attenuates mainly through the excitation and ionization of the matter's atoms. As for the AuNR-TiO_2 nanomotors, the bound electrons of the TiO_2 component are excited to the higher energy level, leading to the conduction band electrons (e_{cb}^-) and valence band holes (h_{vb}^+). Additionally, the Au NRs could be ionized by X-ray irradiation, generating many SEs (such as photoelectrons, Compton and Auger electrons). Based on the energy band levels, the Au–TiO_2 Schottky heterojunction not only significantly promotes the separation of radio-induced e_{cb}^- and h_{vb}^+ but also facilitates the migration of secondary electrons (SEs) from Au NRs to the TiO_2 components. The radio-generated h_{vb}^+ cross the Au–TiO_2 interface, depleting the

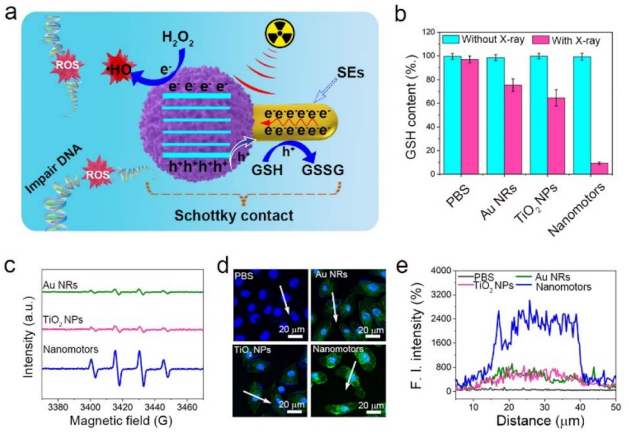

Fig. 4 Radio-induced chemical reactions of the AuNR-TiO_2 nanomotors. (a) Schematic diagram of the mechanism of enhanced radiosensitization combined with ionization and excitation of atoms. (b) Histogram of GSH depletion, (c) EPR spectra, (d) CLSM images of four MCF-7 cell groups treated with different samples after X-ray irradiation for 12 min (X-ray: 50 kV, 80 μA) and (e) their corresponding changes in fluorescence intensity.

overexpressed GSH in the tumor, while the surviving e_{cb}^- reduce H_2O_2 to highly cytotoxic ·OH (Fig. 4a). Since one of the prime functions of the GSH is to maintain the intracellular redox balance, offsetting the ROS-induced antitumor, the depletion of the cellular GSH is conducive to boosting the radiosensitization.[46] Ellman's assay indicated that compared with the Au NR and TiO_2 groups, the Au–TiO_2 nanomotor group exhibited a dramatic decrease in GSH, and the depletion of GSH was more than 90% after 12 min of X-ray irradiation, mainly attributed to the effective transfer of h_{vb}^+ from the valence band of the TiO_2 component to Au NRs through the Schottky heterojunction (Fig. 4b).

The EPR results confirmed that the amount of ·OH generated in the nanomotor group was significantly more than that in the Au NR and pure TiO_2 NP groups, implying the superior separation of radio-induced e_{cb}^- and h_{vb}^+ (Fig. 4c). Subsequently, we further used DCFH-DA to detect ·OH at the cellular level. DCFH-DA is a typical ROS test kit and can be hydrolyzed by esterase to generate DCFH in cells. In the presence of ROS, DCFH could be oxidized into DCF with green fluorescence. As seen in Fig. 4d, upon X-ray radiation, there was no green fluorescence in the PBS group, and weak green fluorescence was observed in the Au NR and TiO_2 NP groups. In contrast, bright green fluorescence was seen in the nanomotor group. The nanomotor group exhibited a nearly six-fold increase in the ·OH concentration than the Au NR and TiO_2 NP groups, with more intense radiosensitization effects (Fig. 4e).

Therapeutic efficacy *in vitro*

The cytotoxic evaluation of the nanomotors with different concentrations was investigated in MCF-7 breast cancer cells and normal LO2 liver cells. In the following cellular experiment, the applied NIR laser intensity was 0.8 W cm^{-2}, each NIR irradiation time was 8 min, the NIR irradiation was carried out in

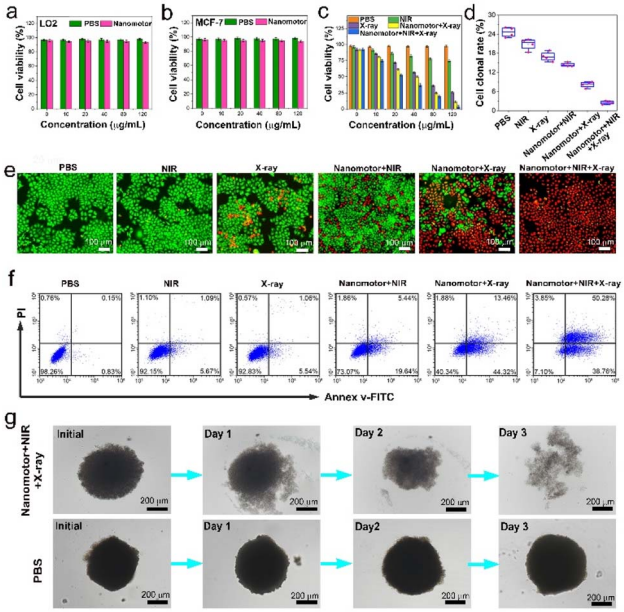

Fig. 5 The therapeutic efficacy *in vitro*. Cell cytotoxicity of nanomotors with different concentrations: (a) LO2 and (b) MCF-7 cells. (c) Cell viability of MCF-7 cells with different treatments. (d) Cell clonal formation rate of MCF-7 cells with different treatments. (e) Live and dead cell fluorescence images of MCF-7 cells stained with Calcein AM/PI, and (f) their flow cytometry analysis with different treatments. (g) Bright-field microscopic images of MCF-7 3D MCSs with different treatments.

three rounds (four rounds for 3D MCSs), and the interval was 20 min. The applied X-ray dose was 4 Gy, the X-ray radiation time was 12 min, and the power was 4 W. As expected, the nanomotors exhibited good biocompatibility and biosafety (Fig. 5aand b). In the CCK-8 cytotoxic test, the PBS, NIR, X-ray, and nanomotor + NIR groups displayed moderate cytotoxicity for MCF-7 breast cancer cells. However, a significant killing effect on cancer cells was found in both the nanomotor + X-ray and the nanomotor + NIR + X-ray groups, reflecting superior radiosensitization of the nanomotors (Fig. 5c). The nanomotor + NIR + X-ray group, in particular, showed a better killing effect than the nanomotor + X-ray group, and >80% of cells were killed as the concentration of the nanomotors was 80 μg mL^{-1}, mainly due to NIR irradiation-driven motion of the nanomotors to intensify cell internalization. Additionally, the cell proliferation ability in different groups was measured through a cell cloning experiment. As shown in Fig. 5d and S13,† the nanomotor + NIR + X-ray group displayed the lowest cell clonal formation rate, suggesting the best killing effect.

The live and dead cell staining and flow cytometry results intuitively demonstrated that the PBS, NIR, and X-ray groups had a negligible killing effect. In contrast, the nanomotor + X-ray group exhibited an excellent cell-killing effect (Fig. 5eand f). As for the nanomotor + NIR + X-ray group, approximately 89% of MCF-7 cells underwent apoptosis after co-incubation with nanomotors (80 μg mL^{-1}) for 24 h, consistent with the CCK-8 cytotoxicity test results (Fig. 5c). In addition, we further evaluated the killing effect of the nanomotor + NIR + X-ray group on 3D MCSs because cell models might be associated with excessively positive treatment outcomes, whereas 3D MCSs are more similar to solid tumors.[47] After three days of treatment, the 3D MCSs in the nanomotor + NIR + X-ray group dissociated, and the PI staining results demonstrated that most cancer cells were dead (Fig. 5g). In contrast, the PBS-treated group exhibited intact 3D cellular spheroids. These findings indicated that under the combination of NIR laser and X-ray irradiation, the nanomotors exhibited a superior antitumor effect on 3D MCSs.

In vivo, NIR-II PAI-guided active motion-enhanced tumor penetration

We employed NIR-II PAI to locate the tumor and monitor the penetration of the nanomotors in the tumor in real-time. MCF-7 subcutaneous tumor models and MC38-luc orthotopic liver tumor models were established, divided into two groups (PBS and AuNR-TiO_2 nanomotor groups), and administrated intravenously with PBS and nanomotors, respectively. The PAI results showed very weak PAI signals at the tumor site in the PBS group. However, the nanomotor group exhibited typical incremental accumulation of the samples at the tumor site, and the PAI signals peaked 24 h after injecting the nanomotors (Fig. 6aand b).

In vivo enhanced tumor penetration of the nanomotors driven by NIR irradiation was confirmed in both a subcutaneous tumor model and an orthotopic liver cancer model by PAI. The applied NIR laser's intensity was 0.8 W cm^{-2}, the NIR irradiation time was 8 min in each round, and the interval was 20 min. As for the subcutaneous tumor model, after intravenous administration of the nanomotors to reach peak accumulation in the absence of NIR irradiation, the nanomotors did not

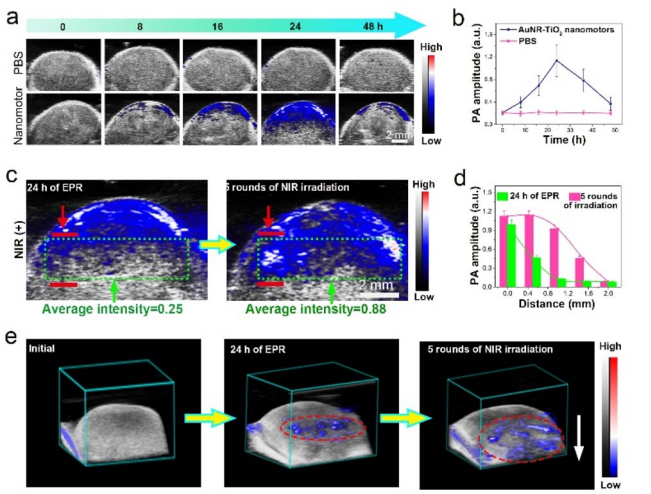

Fig. 6 *In vivo* NIR-II PAI-guided active motion-enhanced tumor penetration. (a) Representative PA images and (b) the curves of PA intensity changing *vs.* time in different groups in the subcutaneous tumor model (excitation at 1250 nm). (c) Representative 2D PA images in the subcutaneous tumor model before and after five rounds of NIR irradiation, and (d) the histogram of PA intensity *vs.* penetration depth, and (e) the corresponding 3D PA images.

display apparently enhanced penetration in the tumor within 4 h based on the analysis of the PA images (Fig. S14†). In contrast, after MCF-7-tumor-bearing mice were irradiated with a NIR laser, apparent deeper penetration and more even distribution of the nanomotors could be observed in the tumor according to the PA images (Fig. 6c). The distance covered by the nanomotors toward the deep tumor site was approximately 1.5 mm after five rounds of NIR irradiation according to the changes in PAI signals (Fig. 6d). The representative 3D PA images in Fig. 6e stereoscopically exhibited the enhanced tumor penetration and more even distribution of the nanomotors driven by NIR irradiation. These PAI results indicate that the active motion of the nanomotors did facilitate their tumor penetration compared with the passive diffusion of the nanoparticles. Similarly, in an orthotopic liver cancer model, the accumulation of the nanomotors increased as a function of time after administration by intravenous injection (Fig. S15†). Compared with the initial state (at 20 h post-injection of samples), after NIR laser irradiation, enhanced penetration and more even distribution of the nanomotors were also observed, with a penetration depth of approximately 1.2 mm after five rounds of NIR irradiation (Fig. S16†). *In vivo* thermal infrared imaging results in Fig. S17† demonstrate that NIR laser irradiation (continuous irradiation for 12 min) did not cause large thermal gradients at the tumor site, consistent with the measurements *in vitro* (Fig. S9†). Thus, the interference of local thermal gradients on the motion of the nanomotors was excluded.

In vivo enhanced radiotherapy effect

As a proof of concept, we further evaluated the radiotherapy effect of the AuNR-TiO_2 nanomotors in both a subcutaneous tumor model and an orthotopic liver cancer model. In the following *in vivo* treatment, 20 h after sample injection, a 0.8 W cm^{-2} NIR laser was first used to continuously irradiate the tumor site five for rounds (each irradiation time is 8 min with an interval of 20 min). Subsequently, an X-ray dose of 4 Gy was applied (X-ray power: 4 W, each irradiation time: 4 min, the interval: 30 min, and three rounds of continuous irradiation). The subcutaneous tumor models were established by inoculating BALB/c mice (~6 weeks old) with MCF-7 tumor cells, and randomly assigned to six groups: (1) PBS, (2) NIR, (3) X-ray, (4) nanomotor + NIR, (5) nanomotor + X-ray, and (6) nanomotor + NIR + X-ray. The administration time was fixed on days 1, 3, 5, and 7, and the administration dosage was 100 μL of samples (4 mg mL^{-1}) each time (Fig. 7a), during treatment.

The tumor in mice could be precisely determined with the guidance of PAI due to the excellent imaging performance of PAI technology, assisting us in applying the NIR and X-ray irradiation. We first investigated the effect of the nanomotors' active motion on the sample biodistribution. As shown in Fig. 7b, blood and muscle had a similar sample distribution on day 1 after injection with or without NIR irradiation at the tumor site. In contrast, at the tumor site, the sample concentration with NIR irradiation was higher than that without NIR irradiation, showing an increase of approximately 1.82 times. The enhanced sample accumulation in the tumor is primarily

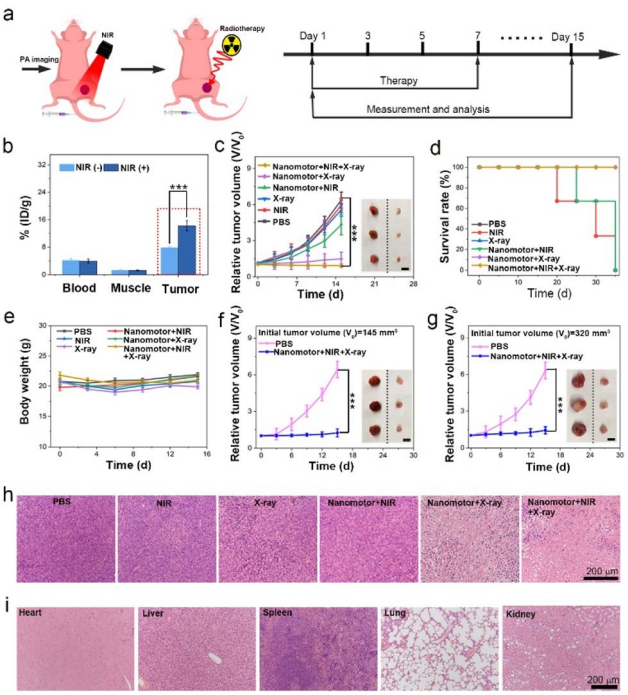

Fig. 7 Enhanced radiotherapy effect of the AuNR-TiO_2 nanomotors on a large tumor. (a) Schematic illustration of construction and treatment of MCF-7-tumor-bearing mice. (b) Sampling biodistribution in different tissues and tumor on day 1 after injection with or without NIR irradiation at the tumor site analyzed by ICP-MS. (c) Tumor growth profiles, (d) survival rate and (e) body weight changing of MCF-7-tumor-bearing mice with an initial tumor volume of 68 mm^3 as a function of time after different treatments. Tumor growth profiles in mice with larger initial tumor volume: (f) V_0 = 145 mm^3 and (g) V_0 = 320 mm^3. The insets are representative photographs of dissected tumors in the PBS group (left) and the nanomotor + NIR + X-ray group (right), respectively. The scale bar is 10 mm. H&E staining of (h) tumor tissue and (i) main organs upon different treatments (V_0 = 68 mm^3). Statistical analysis: *p < 0.1, **p < 0.01, ***p < 0.001.

attributed to the active motion of the nanomotors, which enhanced their penetration, thus preventing their return to circulation. Subsequently, we studied the radiotherapy efficacy of the nanomotors in detail. Compared with the PBS, NIR, X-ray, and nanomotor + NIR groups, both the nanomotor + X-ray and nanomotor + NIR + X-ray groups displayed significant tumor growth inhibition effects after 15 days of treatment (Fig. 7c). Moreover, the survival rate of the mice increased significantly upon radiotherapy (Fig. 7d). In particular, the nanomotor + NIR + X-ray group exhibited the best therapeutic efficacy among these groups, and the tumor inhibition rate reached 75.4% 15 days after treatment, consistent with the cell cytotoxic evaluation assay (Fig. 5d). The superior tumor growth inhibition effect was mainly due to two factors: (1) active motion improved sample accumulation and distribution; (2) the asymmetric Au–TiO_2 heterojunction enhanced radiation dose deposition. Additionally, during the treatment, no significant body weight fluctuations were observed in the mice (Fig. 7e).

Considering the excellent tumor growth inhibition effects in the nanomotor + NIR + X-ray group, we further investigated the

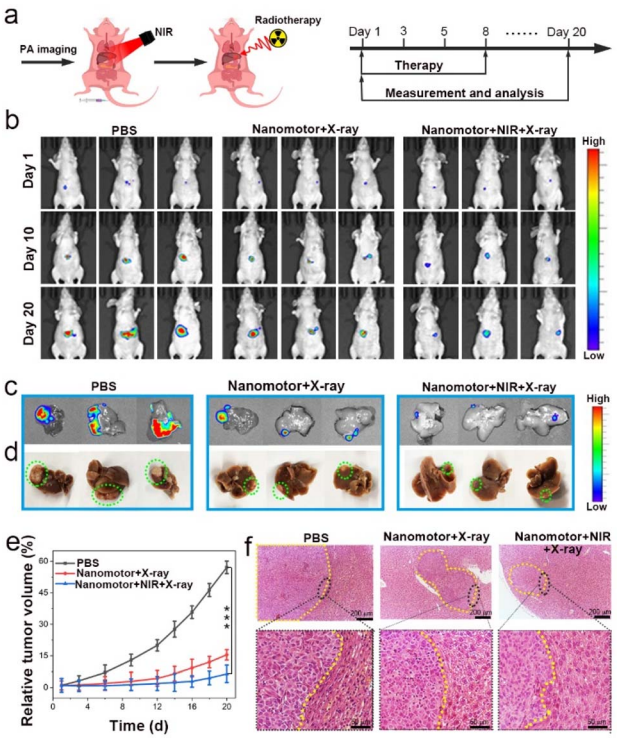

Fig. 8 Orthotopic liver cancer radiotherapy effects of the AuNR-TiO_2 nanomotors. (a) Scheme of the PAI-guided orthotopic liver cancer radiotherapy. (b) Representative bioluminescent photographs of orthotopic liver cancer-bearing mice in different groups on days 1, 10, and 20 with different treatments. The bioluminescence intensity reflected the tumor volume. (c) Bioluminescent images, (d) digital photographs, (e) curves of relative tumor volume as a function of time, and (f) H&E staining results of orthotopic liver tumors *ex vivo* in each group after 20 days of treatment. Statistical analysis: $*p < 0.1$, $**p < 0.01$, $***p < 0.001$.

antitumor effects on tumor-bearing mice with a larger tumor volume (such as 145 and 320 mm^3). As seen in Fig. 7fand g, the nanomotor + NIR + X-ray treatment group also exhibited excellent tumor inhibition effects after 15 days of treatment, even in the mice with a tumor volume as large as 320 mm^3. Additionally, there were no significant body weight changes during treatment, and the survival rate of the mice was improved after treatment (Fig. S18 and S19†). The histological examination (H&E) results demonstrated that most tumor cells were dead without nuclei after treatment, indicating high radiotherapeutic efficacy (Fig. 7h). Furthermore, H&E staining results of the main organ slices reflected that the nanomotors did not apparently harm the main organs, including the heart, liver, spleen, lungs, and kidneys (Fig. 7i). Furthermore, the blood test revealed that the AuNR-TiO_2 nanomotors did not affect the liver and kidney functions after multiple intravenous administrations, suggesting the superior biosafety of the nanomotors (Fig. S20†).

NIR-II PAI guided radiotherapy experiments were carried out in an orthotopic liver cancer model to further explore the potential of these nanomotors in clinical applications. The orthotopic liver tumor-bearing mice were established with MC38-luc cells and were assigned to three groups ($n = 5$ per group): PBS, nanomotor + X-ray, and nanomotor + NIR + X-ray groups. After 20 h post-injection of samples, NIR laser irradiation was applied to drive nanomotors for active penetration, and then X-ray radiotherapy was conducted. The administration time was fixed on days 1, 3, 5, and 8, and the administration dosage was 100 μL (4 mg mL^{-1}) each time. The measurement was made when the fluorescence intensity of the tumor was >5 $\times 10^3$ p s^{-1} cm^{-2} sr^{-1} (Fig. 8a). The first treatment experiment was set to day 1, and then the following treatments were performed at fixed times on days 3, 5, and 8.

The representative bioluminescent images of liver tumor-bearing mice and the bioluminescent and bright-field images of *ex vivo* intact liver from the sacrificed mice on day 20 in Fig. 8b–d show that the tumor growth inhibition effects in the nanomotor + X-ray and nanomotor + NIR + X-ray groups were much better than that in the PBS group. Furthermore, the nanomotor + NIR + X-ray group displayed the best therapeutic efficacy, and the tumor inhibition rate in this group reached 90.3% 20 days after treatment (Fig. 8e). Besides, statistical analysis demonstrated no significant changes in the body weight of orthotopic liver-bearing mice (Fig. S21†), and the survival rate of the mice was improved significantly (Fig. S22†). The tumor area and normal liver tissue were distinguished using a yellow dotted line in H&E staining images, in which densely distributed cells represented the tumor domain (Fig. 8f). The H&E staining results further confirmed that the nanomotor + NIR + X-ray group showed the best tumor growth inhibition effects. Additionally, the H&E staining analysis of main organ slices suggested that the nanomotors did not harm the main organs after treatment (Fig. S23†).

Conclusions

In this work, we developed dandelion-like AuNR-TiO_2 nanomotors by a wet chemistry strategy for NIR-II PAI-guided synergistically enhanced cancer radiotherapy. The non-centrosymmetric nanostructure of the nanomotor generates stronger local plasmonic near-fields close to the Au–TiO_2 interface, and the Au–TiO_2 heterojunction greatly facilitates the charge separation and migration, allowing for strongly plasmon-enhanced photocatalytic activity. The nanomotors exhibit superior motility both *in vitro* and *in vivo*, propelled by H_2 generated *via* NIR-catalysis on one side of Au nanorod. Specifically, with the guidance of PAI, approximately 1.5 and 1.2 mm of displacements for the nanomotors are measured in a subcutaneous tumor model and an orthotopic liver cancer model, respectively, driven by NIR irradiation. The active motion of the nanomotors effectively prevents the samples from returning to the bloodstream to improve the sample accumulation in the tumor significantly. Additionally, a high radiation dose deposition is confirmed in the form of more $^{\bullet}OH$ generation and much glutathione depletion. The Janus nanomotors perfectly integrate the feature of improved sample accumulation with enhanced radiation energy deposition, resulting in a significant radiotherapy tumoricidal effect, which is verified both in a subcutaneous tumor model and an orthotopic liver cancer

model. It is believed that the rational design of multifunctional Janus nanomotors will pave the way for the development of the next generation of radiosensitizers.

Ethical statement

All the animal experimental procedures were in accord with the guidelines of the Regional Ethics Committee for Animal Experiments and the Care Regulations approved by the Institutional Animal Care and Use Committee of Fuzhou University.

Data availability

All data related to this work have been presented in the manuscript or ESI.† We have no more experimental or computational data associated with this article.

Author contributions

L. L. conducted the experiments and finished the manuscript with the assistance of Q. L., Y. W., Z. W. and J. Y. provided assistance to conduct PAI and USI tests. Q. F., L. S. and X. Z. contributed to establishment of the mouse model. H. H. and H. Y. offered some help in writing. Prof. J. S., L. S, X. Z., Z. Y. and L. C. provided constructive guidance for the subject design and experiments.

Conflicts of interest

There are no conflicts to declare.

Acknowledgements

This research was supported by the National Key Research and Development Program of China (2020YFA0210800), the National Natural Science Foundation of China (No. 22027805, U21A20377, and 21874024), the Major Project of Science and Technology of Fujian Province (2020HZ06006), the joint research projects of Health and Education Commission of Fujian Province (No. 2019-WJ-20), China Postdoctoral Science Foundation (No. 2021M690642), and the Natural Science Foundation of Fujian Province (No. 2020J02012).

Notes and references

1 W. Tang, Z. Yang, L. He, L. Deng, P. Fathi, S. Zhu, L. Li, B. Shen, Z. Wang, O. Jacobson, J. Song, J. Zou, P. Hu, M. Wang, J. Mu, Y. Cheng, Y. Ma, L. Tang, W. Fan and X. Chen, *Nat. Commun.*, 2021, **12**, 523.
2 M. Gao, C. Liang, X. Song, Q. Chen, Q. Jin, C. Wang and Z. Liu, *Adv. Mater.*, 2017, **29**, 1701429.
3 Y. Yang, M. Chen, B. Wang, P. Wang, Y. Liu, Y. Zhao, K. Li, G. Song, X.-B. Zhang and W. Tan, *Angew. Chem., Int. Ed.*, 2019, **58**, 15069–15075.
4 Y. Chen, H. Zhong, J. Wang, X. Wan, Y. Li, W. Pan, N. Li and B. Tang, *Chem. Sci.*, 2020, **11**, 6098.
5 Z. Zhao, P. Gao, L. Ma and T. Chen, *Chem. Sci.*, 2020, **11**, 3780–3789.
6 D. Xia, D. Hang, Y. Li, W. Jiang, J. Zhu, Y. Ding, H. Gu and Y. Hu, *ACS Nano*, 2020, **14**, 15654–15668.
7 H. Huang, C. Zhang, X. Wang, J. Shao, C. Chen, H. Li, C. Ju, J. He, H. Gu and D. Xia, *Nano Lett.*, 2020, **20**, 4211–4219.
8 K. Ni, G. Lan, Y. Song, Z. Hao and W. Lin, *Chem. Sci.*, 2020, **11**, 7641–7653.
9 C. Zhang, L. Yan, Z. Gu and Y. Zhao, *Chem. Sci.*, 2019, **10**, 6932–6943.
10 J. Xie, L. Gong, S. Zhu, Y. Yong, Z. Gu and Y. Zhao, *Adv. Mater.*, 2019, **31**, 1802244.
11 S.-S. Li, A.-J. Wang, P.-X. Yuan, L.-P. Mei, L. Zhang and J.-J. Feng, *Chem. Sci.*, 2022, **13**, 5505–5530.
12 J. Ding, J. Chen, L. Gao, Z. Jiang, Y. Zhang, M. Li, Q. Xiao, S. S. Lee and X. Chen, *Nano Today*, 2019, **29**, 100800.
13 M. M. Wan, H. Chen, Z. Wang, Z. Y. Liu, Y. Q. Yu, L. Li, Z. Y. Miao, X. W. Wang, Q. Wang, C. Mao, J. Shen and J. Wei, *Adv. Sci.*, 2021, **8**, 12.
14 Y. Wang, S. Luo, Y. Wu, P. Tang, J. Liu, Z. Liu, S. Shen, H. Ren and D. Wu, *ACS Nano*, 2020, **14**, 17046–17062.
15 F. Xu, X. Huang, Y. Wang and S. Zhou, *Adv. Mater.*, 2020, **32**, 1906745.
16 H.-J. Li, J.-Z. Du, X.-J. Du, C.-F. Xu, C.-Y. Sun, H.-X. Wang, Z.-T. Cao, X.-Z. Yang, Y.-H. Zhu, S. Nie and J. Wang, *Proc. Natl. Acad. Sci. U. S. A.*, 2016, **113**, 4164–4169.
17 S. Tang, F. Zhang, H. Gong, F. Wei, J. Zhuang, E. Karshalev, B. Esteban-Fernández de Ávila, C. Huang, Z. Zhou, Z. Li, L. Yin, H. Dong, R. H. Fang, X. Zhang, L. Zhang and J. Wang, *Sci. Robot.*, 2020, **5**, eaba6137.
18 Y. Wang, W. Duan, C. Zhou, Q. Liu, J. Gu, H. Ye, M. Li, W. Wang and X. Ma, *Adv. Mater.*, 2019, **31**, 1970363.
19 M. Yan, L. Xie, J. Tang, K. Liang, Y. Mei and B. Kong, *Chem. Mater.*, 2021, **33**, 3022–3046.
20 C. Gao, Y. Wang, Z. Ye, Z. Lin, X. Ma and Q. He, *Adv. Mater.*, 2021, **33**, 2000512.
21 Z. Wu, J. Troll, H.-H. Jeong, Q. Wei, M. Stang, F. Ziemssen, Z. Wang, M. Dong, S. Schnichels, T. Qiu and P. Fischer, *Sci. Adv.*, 2018, **4**, eaat4388.
22 J. Shao, S. Cao, D. S. Williams, L. K. E. A. Abdelmohsen and J. C. M. van Hest, *Angew. Chem., Int. Ed.*, 2020, **59**, 16918–16925.
23 J. Wang, Z. Xiong, M. Liu, X.-m. Li, J. Zheng, X. Zhan, W. Ding, J. Chen, X. Li, X. D. Li, S.-P. Feng and J. Tang, *ACS Nano*, 2020, **14**, 3272–3280.
24 M. Valdez-Garduño, M. Leal-Estrada, E. S. Oliveros-Mata, D. I. Sandoval-Bojorquez, F. Soto, J. Wang and V. Garcia-Gradilla, *Adv. Funct. Mater.*, 2020, **30**, 2004043.
25 S. Cao, J. Shao, H. Wu, S. Song, M. T. De Martino, I. A. B. Pijpers, H. Friedrich, L. K. E. A. Abdelmohsen, D. S. Williams and J. C. M. van Hest, *Nat. Commun.*, 2021, **12**, 2077.
26 Z. Lin, C. Gao, D. Wang and Q. He, *Angew. Chem., Int. Ed.*, 2021, **60**, 8750–8754.
27 P. Díez, E. Lucena-Sánchez, A. Escudero, A. Llopis-Lorente, R. Villalonga and R. Martínez-Máñez, *ACS Nano*, 2021, **15**, 4467–4480.

28 S. Wang, K. Liu, Q. Zhou, C. Xu, J. Gao, Z. Wang, F. Wang, B. Chen, Y. Ye, J. Ou, J. Jiang, D. A. Wilson, S. Liu, F. Peng and Y. Tu, *Adv. Funct. Mater.*, 2021, **31**, 2009475.
29 S. Zheng, Y. Wang, S. Pan, E. Ma, S. Jin, M. Jiao, W. Wang, J. Li, K. Xu and H. Wang, *Adv. Funct. Mater.*, 2021, 2100936.
30 Y. Ji, X. Lin, Z. Wu, Y. Wu, W. Gao and Q. He, *Angew. Chem., Int. Ed.*, 2019, **58**, 12200–12205.
31 M. Wan, T. Li, H. Chen, C. Mao and J. Shen, *Angew. Chem., Int. Ed.*, 2021, **60**, 13158–13176.
32 I. A. B. Pijpers, S. Cao, A. Llopis-Lorente, J. Zhu, S. Song, R. R. M. Joosten, F. Meng, H. Friedrich, D. S. Williams, S. Sánchez, J. C. M. van Hest and L. K. E. A. Abdelmohsen, *Nano Lett.*, 2020, **20**, 4472–4480.
33 A. Serrà and J. García-Torres, *Appl. Mater. Today*, 2021, **22**, 100939.
34 J. Huang and K. Pu, *Angew. Chem., Int. Ed.*, 2020, **59**, 11717–11731.
35 M. Y. Lucero, A. K. East, C. J. Reinhardt, A. C. Sedgwick, S. Su, M. C. Lee and J. Chan, *J. Am. Chem. Soc.*, 2021, **143**, 7196–7202.
36 Y.-S. Chen, Y. Zhao, S. J. Yoon, S. S. Gambhir and S. Emelianov, *Nat. Nanotechnol.*, 2019, **14**, 465–472.
37 J. Chen, A. C. Sedgwick, S. Sen, Y. Ren, Q. Sun, C. Chau, J. F. Arambula, T. Sarma, L. Song, J. L. Sessler and C. Liu, *Chem. Sci.*, 2021, **12**, 9916–9921.
38 H. Gu, W. Liu, W. Sun, J. Du, J. Fan and X. Peng, *Chem. Sci.*, 2022, **13**, 9719–9726.
39 C. Zhang, Z. Qiu, L. Zhang, Q. Pang, Z. Yang, J.-K. Qin, H. Liang and S. Zhao, *Chem. Sci.*, 2021, **12**, 4883–4888.
40 C. Xu, Y. Wang, E. Wang, N. Yan, S. Sheng, J. Chen, L. Lin, Z. Guo, H. Tian and X. Chen, *Adv. Funct. Mater.*, 2021, **31**, 2009314.
41 Z. Li, Z. Wang, J. Li, Q. Zhu, Z. Wang and Z. Dai, *J. Am. Chem. Soc.*, 2021, **143**, 13478–13482.
42 D. Wang, H. Wang, L. Ji, M. Xu, B. Bai, X. Wan, D. Hou, Z.-Y. Qiao, H. Wang and J. Zhang, *ACS Nano*, 2021, **15**, 8694–8705.
43 H. Chen, T. Shi, Y. Wang, Z. Liu, F. Liu, H. Zhang, X. Wang, Z. Miao, B. Liu, M. Wan, C. Mao and J. Wei, *J. Am. Chem. Soc.*, 2021, **143**, 12025–12037.
44 J. Yang, J. Zheng, R. Ai, Y. Lai, T. H. Chow, L. Shao and J. Wang, *Angew. Chem., Int. Ed.*, 2021, **60**, 24958–24967.
45 L. Vigderman and E. R. Zubarev, *Chem. Mater.*, 2013, **25**, 1450–1457.
46 R. Cai, H. Xiang, D. Yang, K.-T. Lin, Y. Wu, R. Zhou, Z. Gu, L. Yan, Y. Zhao and W. Tan, *J. Am. Chem. Soc.*, 2021, **143**, 16113–16127.
47 M. Chiba, Y. Ichikawa, M. Kamiya, T. Komatsu, T. Ueno, K. Hanaoka, T. Nagano, N. Lange and Y. Urano, *Angew. Chem., Int. Ed.*, 2017, **56**, 10418–10422.